







**Measurement of the neutron-induced capture-to-fission cross section ratio in  $^{233}\text{U}$  at LANSCE**

E. Leal-Cidoncha <sup>\*</sup>, A. Couture, E. M. Bond, T. A. Bredeweg , C. Fry , T. Kawano ,  
A. E. Lovell , G. Rusev, I. Stetcu , and J. L. Ullmann  
*Los Alamos National Laboratory, Los Alamos, New Mexico 87545, USA*

L. Leal

*Institut de Radioprotection et de Sûreté Nucléaire, 92262 Fontenay aux Roses, Cedex, France*

M. T. Pigni

*Oak Ridge National Laboratory, Oak Ridge, Tennessee 37831-6171, USA*



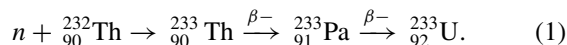
(Received 23 January 2023; accepted 13 June 2023; published 19 July 2023)

The neutron-induced capture-to-fission cross section ratio of  $^{233}\text{U}$  has been measured at the Los Alamos Neutron Science Center at Los Alamos National Laboratory in the energy range from 0.7 eV to 250 keV. The detector setup combines the Detector for Advanced Neutron Capture Experiments (DANCE) to measure  $\gamma$  rays generated from both capture and fission reactions, and the neutron detector array at DANCE to measure fission neutrons. This is the first measurement of the capture-to-fission ratio between 2 and 30 keV. The evaluations are in good agreement with the results in the resolved resonance region. In both the unresolved resonance region and the fast neutron region, a lower capture-to-fission ratio is obtained in this work from 10 to 150 keV compared to current evaluations, while good agreement with the experimental data and the evaluations is found above 150 keV. Statistical model calculations were performed to compare with the experimental data. Significantly reduced  $\langle\Gamma_\gamma\rangle$  was required to reproduce the measured data.

DOI: [10.1103/PhysRevC.108.014608](https://doi.org/10.1103/PhysRevC.108.014608)

## I. INTRODUCTION

Fissile properties of  $^{233}\text{U}$  play a key role in the Th-U fuel cycle, which has been proposed as an alternative to the commonly adopted U-Pu fuel cycle. There are several advantages to the Th-U fuel cycle over other schemes. First, Th has a higher natural abundance than U. Second, the operation of the cycle produces fewer transuranic elements, reducing proliferation concerns and making operation and disposal safer. Uranium-233 is generated by transmutation of  $^{233}\text{Th}$  that is generated from  $^{232}\text{Th}$  by neutron absorption as shown in Eq. (1). The Th-U fuel cycle may be the basis of thermal breeder reactors as well as suitable for fast reactors:



The experimental  $^{233}\text{U}(n, \gamma)$  cross section data available in the literature are scarce [1–3] and were measured before recent advances in data acquisition and detector technology. An accurate determination of the  $^{233}\text{U}(n, \gamma)$  cross section is required by the Nuclear Criticality Safety Program (NCSP)

to complete the neutron-induced cross section data due to an underestimation in reactivity for thermal solutions. Further, a new evaluation by Pigni *et al.* [4] reported the need of  $^{233}\text{U}$  capture data.

The capture-to-fission cross section ratio ( $\alpha$ ) is a more reliable quantity experimentally than the absolute cross section as the systematic uncertainties derived from the neutron flux, the sample mass, and self-shielding cancel out. Recent work [5] has placed the fission cross section on a firm basis. The  $\alpha$  ratio calculated from the existing capture and fission cross section data from the EXFOR database is shown in Fig. 1. The capture and fission cross section in the energy range from 0.4 eV to 2 keV were measured with the electron linear accelerator at Rensselaer Polytechnic Institute (RPI) using a liquid scintillator tank combined with a fission chamber in 1968 [2]. Another measurement of the capture and fission cross section was performed at the neutron time-of-flight facility (n\_TOF) at CERN using the Total Absorption Calorimeter (TAC) [1]; data from this measurement were reported to EXFOR from 0.7 to 1000 eV in two datasets with different energy resolutions. Hopkins *et al.* measured the capture-to-fission ratio from 30 keV to 1 MeV using a scintillator tank consisting in a 1 m long and 1 m diameter cylinder [3]. Finally, a more recent measurement of the capture-to-fission ratio in the neutron energy range from 1 eV to 1 keV has been performed at n\_TOF using the TAC and a fission chamber, although their data are still preliminary and not available [6].

\*ealcid@lanl.gov

Published by the American Physical Society under the terms of the [Creative Commons Attribution 4.0 International](https://creativecommons.org/licenses/by/4.0/) license. Further distribution of this work must maintain attribution to the author(s) and the published article's title, journal citation, and DOI.

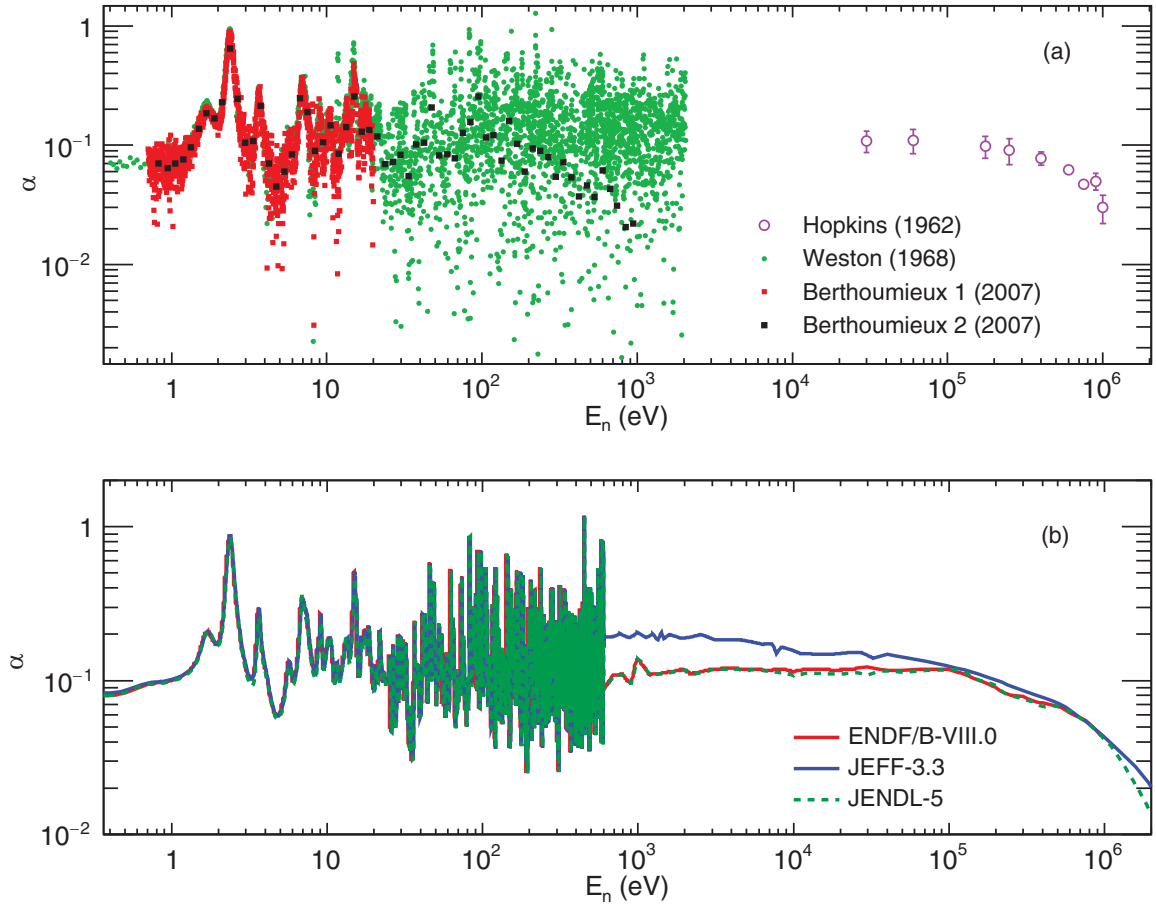


FIG. 1. (a) Existing capture-to-fission ratio data in  $^{233}\text{U}$ , from Weston (1968) [2], Berthoumieux *et al.* (2007) [1], and Hopkins and Diven (1962) [3]. (b) capture-to-fission ratio from ENDF/B-VIII.0, JEFF-3.3, and JENDL-5.

The evaluated data show a good agreement in the resolved resonance region up to 600 eV. ENDF/B-VII.1 and JEFF-3.3 are identical. ENDF/B-VIII.0 adopted the capture and fission cross sections from JENDL-4, which improved the agreement with Hopkins and Diven. Fission is very similar among the three libraries including the latest JENDL-5, which slightly differs in fission from JENDL-4. The main change is observed in the capture cross section. In both the unresolved resonance region and fast neutron region discrepancies are found between ENDF/B-VIII.0 and JEFF-3.3, while JENDL-5 is in general good agreement with ENDF/B-VIII.0, as shown in Fig. 1(bottom). One should note that the ENDF/B-VIII.0 library adopted the  $^{233}\text{U}$  evaluation from JENDL-4.0 with some minor adjustments. In order to better understand the discrepancies in the unresolved resonance region, a measurement of the capture-to-fission cross section ratio on  $^{233}\text{U}$  between 2–30 keV would be needed, as there are no experimental data in that energy range. Also, above 30 keV the only available experimental data were measured by Hopkins and Diven providing only nine data points between 30 keV and 1 MeV. New experimental data would provide more information on the ratio above 30 keV.

The challenge in this measurement lies in the difficulty of measuring capture cross section data due to the competing fission channel. Since a fission event is about one order of

magnitude more likely than a capture event, the measurement of the  $^{233}\text{U}(n, \gamma)$  cross section strongly relies on the ability to disentangle the  $\gamma$  rays produced in capture and fission reactions. Therefore, an experimental setup combining capture and fission detectors is preferred.

Following this requirement, a new measurement has been performed at LANSCE combining the Detector for Advanced Neutron Capture Experiments (DANCE)  $\gamma$  calorimeter with the neutron detector array at DANCE (NEUANCE), to identify neutron-induced capture and fission events, respectively. Measuring the fission neutrons instead of the fission fragments allowed the use of a thick  $^{233}\text{U}$  target in this experiment, reducing the required neutron beam time.

## II. EXPERIMENTAL SETUP

Neutron-induced capture experiments are carried out at LANSCE using the DANCE  $\gamma$ -ray calorimeter. Neutrons are produced at LANSCE via spallation reactions caused by an 800 MeV proton beam with a repetition rate of 20 Hz hitting a tungsten target. A more detailed description of the LANSCE facility, can be found in Ref. [7]. The DANCE setup is located at the Flight Path 14 of the Lujan Neutron Scattering Center, at  $\sim 20$  m from the spallation target, where water is used to moderate the fast neutrons before entering the flight path.

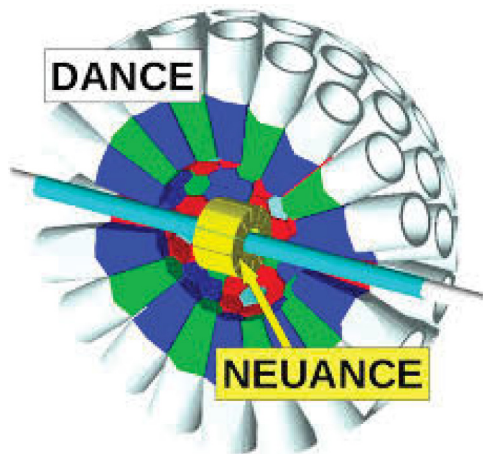


FIG. 2. NEUANCE detector placed inside the DANCE detector's inner cavity.

One of the limitations when measuring the capture  $\gamma$  rays is the background produced by fission  $\gamma$  rays. This background is especially large in the case of the  $^{233}\text{U}$  and has to be properly studied and subtracted. For this reason, a setup combining capture and fission detectors was used to accurately measure the capture cross section. By combining these two detectors, the fission events can be translated into coincidence events between the two detectors, and used to tag the fission  $\gamma$  rays, generating a fission spectrum that can be subtracted from the total  $\gamma$ -ray spectrum.

The DANCE detector is an array composed of 160  $\text{BaF}_2$  crystals [8] covering a solid angle of approximately  $3.5\pi$  with a single  $\gamma$ -ray efficiency of 85%. The design can hold 162 crystals, of which 160 crystals are set in place and two spaces have been left empty for the beam pipe. The crystals are in four shapes, each 15 cm deep and covering the same solid angle. The sample under study is placed in the center of DANCE, under vacuum in the interior of the beam pipe [9].

The NEUANCE detector consists of 21 stilbene crystals arranged in a cylindrical geometry around the beam pipe, placed inside the DANCE inner cavity, see Fig. 2. A  $^{\text{nat}}\text{Li}$ -loaded polyethylene shell has been placed inside the DANCE inner cavity, between NEUANCE and DANCE, in order to reduce the scattered background from the neutrons hitting the sample backing. The NEUANCE efficiency for a single fission neutron is 12.5%. NEUANCE detects neutrons with energies above 500 keV, which includes a significant fraction of the fission neutron energy spectrum. Scattered neutrons have energies below this threshold and are not detected. A more detailed description of the detectors can be found in Refs. [9,10].

The neutron flux at the Lujan Center in the hundred kiloelectronvolt neutron energy region requires the use of a thick sample in order to achieve sufficient statistics during a viable measuring time. One of the advantages of measuring fission reactions by detecting the fission neutrons instead of the fission fragments is the possibility of using a thick target, thus reducing the required beam time. A 20 mg  $^{233}\text{U}$  sample in the form of solid oxide was fabricated at LANL for this ex-

TABLE I. Isotopic composition. Materials with less than 1 ppm are not reported.

Isotope	Atom (%)
$^{233}\text{U}$	99.9843
$^{234}\text{U}$	<0.0002
$^{235}\text{U}$	0.0017
$^{236}\text{U}$	0.0004
$^{238}\text{U}$	0.0134

periment. The sample material isotopic composition is given in Table I. The nominal 5 mm diameter sample was stippled on a 0.3 mil Kapton tape, sealed by another Kapton tape, and introduced in a standard DANCE target holder. Note that the ratio method used in this work is not sensitive to the exact sample geometry. The container with the sample was placed inside the neutron beam pipe in the center of the DANCE inner cavity.

The DANCE Data Acquisition System (DAQ) is implemented in the Maximum Integrated Data Acquisition System (MIDAS) framework [11] and the data acquisition front-end software is available through GitHub [12]. The data acquisition technique is discussed in more detail elsewhere [13]. Each detector, including the  $\text{BaF}_2$  crystals, the NEUANCE scintillators, and the beam monitors, are individually digitized with CAEN VX1730B 14-bit, 500 MS/s waveform digitizers using the digital pulse processing-pulse shape discrimination (DPP-PSD) digitizer firmware. For the DANCE crystals, a short gate of 12 ns (six samples) and long gate of 800 ns (400 samples) was used. For each event, the short integral, the long integral, a baseline value, and a timestamp is recorded. In addition, 48 samples of the waveform are written to file, starting approximately 16 samples before the event trigger. This additional waveform snippet allows for an improved determination of the event time and pileup in offline analysis. A total of fourteen digitizers, each with sixteen channels, comprise the DAQ hardware. The digitizers are all run with a single clock to ensure consistent time-of-flight determination. Finally, a T0 signal, corresponding to the initiation of the neutron pulse—and its timestamp—is recorded. All 14 digitizers deliver data to a single master computer with an attached RAID for data storage and run synchronization.

### III. DATA ANALYSIS

The data analysis involves event building, neutron energy calculation, energy calibration, fission event identification, background subtraction, and calculation of the capture-to-fission ratio. The data analysis code can be found on GitHub, however, the customizations made to create coincidences between DANCE and NEUANCE are not included in the default distribution [14].

A physics event is defined by all detector signals found within a coincidence window of 10 ns for the DANCE crystals and 25 ns for coincidences between DANCE and NEUANCE. The  $\gamma$  rays are characterized with DANCE by the total energy and their multiplicity. The total energy ( $E_{\text{tot}}$ ) is the  $\gamma$ -ray energy deposited in a group of crystals in an event, and the

multiplicity is the number of crystals fired when an event happens. Because of the high segmentation of the DANCE array, a  $\gamma$  ray which interacts with one crystal has a high probability to deposit only part of its energy in that crystal, depositing the remainder in one or more neighboring crystals. To account for this, in a single physics event, crystals are dynamically grouped into “clusters” of neighboring crystals that all saw a  $\gamma$  ray. This allows definition of a cluster multiplicity  $M_{cl}$  in addition to the crystal multiplicity  $M_{cr}$ , where  $M_{cl} \leq M_{cr}$  by definition. From this definition of a cluster, we define a cluster energy  $E_{cl}$  to be the sum of the energies of the constituent crystals  $E_{cr}$ . In such a way  $E_{tot} = \Sigma E_{cr} = \Sigma E_{cl}$ . Past studies of the instrument have shown that the cluster multiplicity and energy more accurately reflect the emitted  $\gamma$ -ray multiplicity and energy than the crystal multiplicity and energy for events with relatively low true multiplicity [15].

### A. Neutron energy calculation

The incident neutron energy is calculated by using the time-of-flight technique, which consists in measuring the time that a neutron takes to travel from the neutron source to the reaction sample knowing the distance between both. The neutron energy is calculated using the relativistic equation

$$E_n = m_n c^2 \frac{1}{\sqrt{1 - \left(\frac{v}{c}\right)^2}}, \quad \text{with } v = \frac{L}{t}. \quad (2)$$

For neutron energies below 1 MeV this simplified to the well-known nonrelativistic equation

$$E_n = \frac{1}{2} m_n v^2, \quad (3)$$

where  $E_n$  is the neutron energy,  $m_n$  is the mass of the neutron,  $v$  is the neutron velocity,  $L$  is the flight path length,  $c$  is the speed of light, and  $t$  refers to the “measured” time of flight.

The moderation of neutrons in the moderator introduces a moderation time factor  $\Delta t$  that depends on the neutron energy and has to be accounted for in the equations. The “measured” time of flight is the sum of the “actual” time of flight of the neutron and the moderation time. The moderation time  $\Delta t$  is energy dependent and has been determined through a simulation of the target-moderator assembly at the surface of the moderator [16].

### B. Detector calibration

Pulse shape discrimination (PSD) has been used to separate  $\gamma$  rays from  $\alpha$  particles in DANCE, and  $\gamma$  rays from neutrons in NEUANCE.

The DANCE crystals have been calibrated using  $\gamma$ -ray sources and the intrinsic radioactivity of the  $\text{BaF}_2$ .  $\text{BaF}_2$  scintillation light has a fast and a slow component. The ratio between them is very different for  $\gamma$  rays and  $\alpha$  particles allowing particle identification, as can be seen in Fig. 3. The short and long integrals in DANCE signals correspond to charge integration over 12 and 800 ns, respectively. This clear separation between  $\gamma$  rays and  $\alpha$  particles allows the use of the  $\alpha$ -decay chain of the chemical homologue  $^{226}\text{Ra}$  present in the crystals for calibration, see Fig. 4.

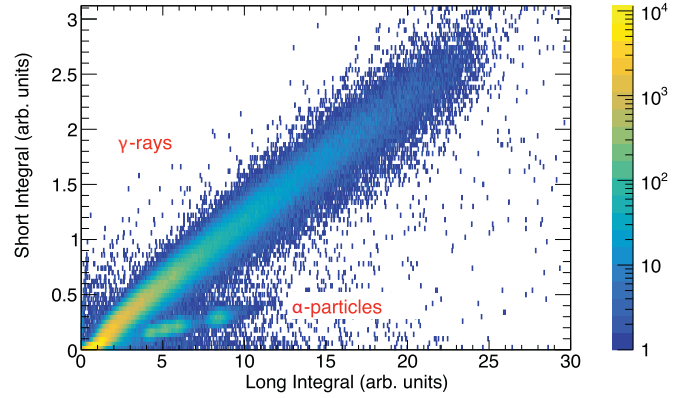


FIG. 3. PSD spectrum for one of the DANCE crystals. The  $\alpha$  particle spectrum is selected and used for the DANCE crystals energy calibration.

NEUANCE detects neutrons. Good discrimination between the two is required. Figure 5 shows this clear separation. Two lines of events can be observed in the figure, the events on the top correspond to neutrons and the events on the bottom to  $\gamma$  rays. The NEUANCE crystals were calibrated using the  $\gamma$ -source peaks in the spectra, see Fig. 6.

### C. Fission background

The  $\gamma$ -ray background generated from the fission process is identified by searching for coincidences between the DANCE  $\gamma$  rays and NEUANCE neutron signals. The events from DANCE found in coincidence with NEUANCE neutrons were tagged as fission events. However as the efficiency of NEUANCE is not 100%, the remaining fission background has to be identified and subtracted. Figure 7 shows the tagged DANCE fission events on the top figure and the untagged DANCE events on the bottom, this last one clearly

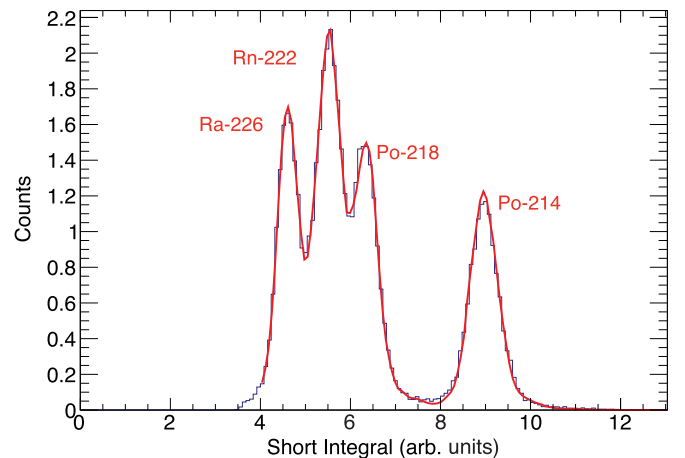


FIG. 4. DANCE  $\alpha$ -particle spectrum for one of the DANCE crystals fitted to a sum of Gaussian distribution (in red) used for the energy calibration. The peaks correspond to the  $\alpha$ -particle decays of  $^{226}\text{Ra}$  (4.8 MeV),  $^{222}\text{Rn}$  (5.5 MeV),  $^{218}\text{Po}$  (6.0 MeV), and  $^{214}\text{Po}$  (7.7 MeV).

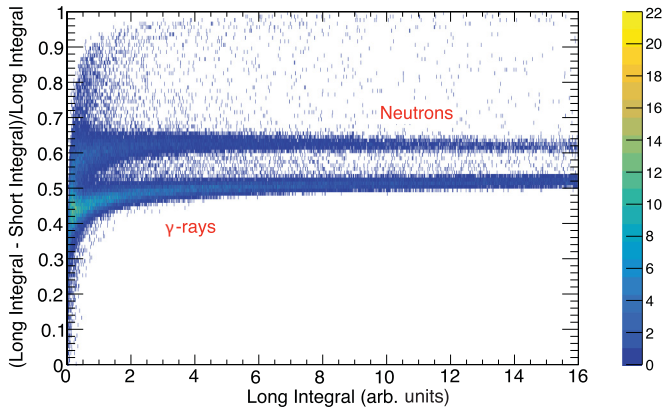


FIG. 5. PSD spectrum for one of the NEUANCE crystals showing the good separation between fission neutrons (top events) and  $\gamma$  rays (bottom events).

showing the remaining fission background. This remaining fission background subtraction is performed normalizing the tagged fission  $\gamma$ -ray spectrum to the total spectrum inside a normalization window for high cluster multiplicities, where exclusively fission events are found (see Fig. 7). As the shape of the fission spectrum does not change over the incident neutron energy range of interest, in order to reduce the statistical fluctuations, the shape of the tagged spectrum with incident neutron energies from 3 to 30 eV has been normalized and used to subtract the remaining fission background for each neutron energy bin.

#### D. Other sources of background

One of the main sources of background comes from scattered neutrons inducing capture reactions, primarily on Barium, in the DANCE crystals. These capture reactions occur on  $^{134}\text{Ba}$ ,  $^{135}\text{Ba}$ ,  $^{136}\text{Ba}$ ,  $^{137}\text{Ba}$ , and  $^{138}\text{Ba}$  with  $Q$  values of 6.972, 9.108, 6.906, 8.612, and 4.723 MeV, respectively, producing peaks in the total energy spectrum at these energies. The  $^{\text{nat}}\text{Li}$ -loaded polyethylene shell placed between NEUANCE and DANCE reduces the scattered background, however it does not completely eliminate it. This scattering background dominates at cluster multiplicities below 3, and the fission background dominates at multiplicities 6 and above. The background subtraction was performed selecting the events from DANCE with cluster multiplicities 4 and 5 inside the capture range. The total energy of the  $\gamma$  rays showing the raw data per incident neutron energy for the different components of the background, is shown in Fig. 8. The neutron scattering spectrum was obtained using a  $^{208}\text{Pb}$  sample. As the background varies with the incident neutron energy, it was calculated and subtracted as a function of  $E_n$ . The  $Q$ -value peak for  $^{233}\text{U}$  is 6.845 MeV. Fission  $\gamma$  rays dominate at low total energies, as seen in red in Fig. 8. The scattering peak between 7.5–9.5 MeV was used to normalize the scattering background distribution to the fission-suppressed spectrum. The  $\beta$ -delayed fission  $\gamma$  spectrum was obtained by taking data prior to the proton beam pulse in the time-of-flight spectrum. It was normalized for each energy bin using the

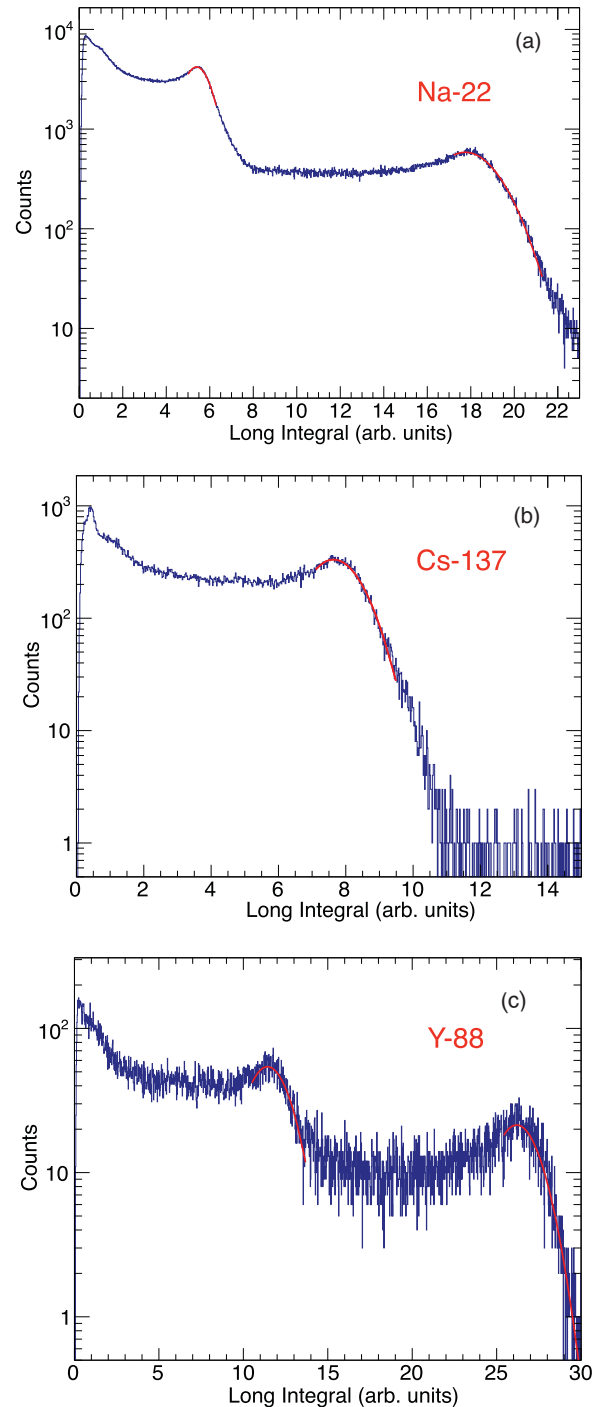


FIG. 6. (a)  $^{22}\text{Na}$   $\gamma$ -ray spectrum with two peaks at 511 keV and 1274.537 keV. (b)  $^{137}\text{Cs}$   $\gamma$ -ray spectrum with a peak at 661.657 keV. (c)  $^{88}\text{Y}$   $\gamma$ -ray spectrum with two peaks at 898.047 keV and 1836.090 keV. All the figures correspond to one of the NEUANCE crystals. The peaks in the spectra have been fitted to Gaussian distribution (in red).

corresponding time width of the bin. The number of capture events per neutron energy bin were calculated as the integral of the background-suppressed total energy spectrum between 5.9 and 7 MeV (around the  $Q$ -value peak for  $^{233}\text{U}$ ).

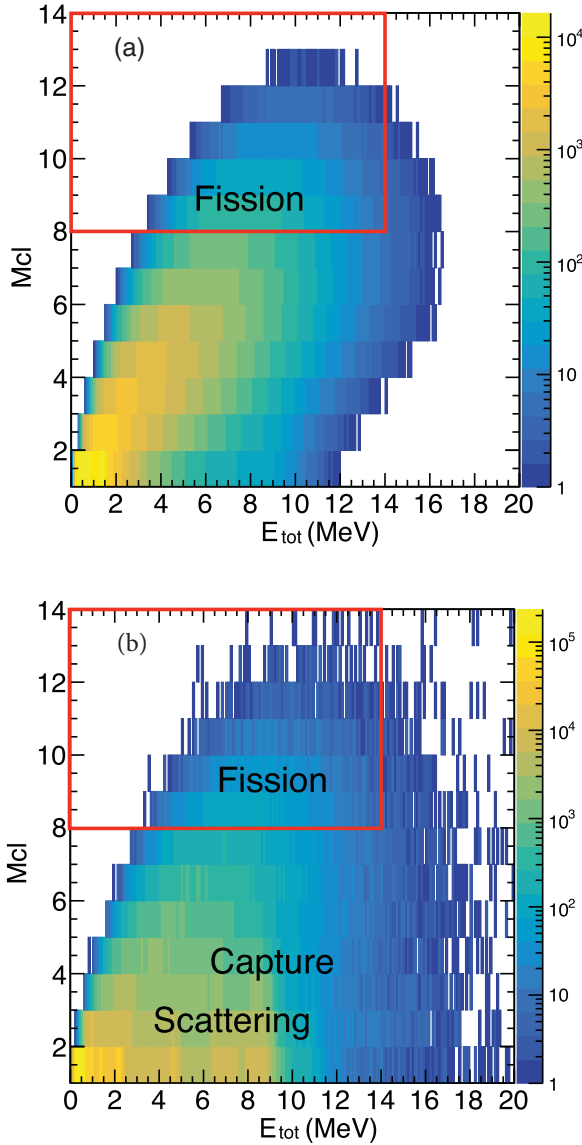


FIG. 7. (a) Cluster multiplicity as a function of the total energy of the  $\gamma$ 's showing the tagged events and (b) the untagged events. The regions where fission, capture and scattering events are dominant are labeled in the figure. The fission normalization window is indicated by the red rectangle.

### E. Capture-to-fission ratio

The capture-to-fission ratio, commonly denoted  $\alpha(E_n)$ , is given by the ratio of the energy-dependent neutron capture cross section and the neutron-induced fission cross section

$$\alpha(E_n) \equiv \frac{\sigma_\gamma(E_n)}{\sigma_f(E_n)}. \quad (4)$$

In the case of relatively low neutron energies, where the total cross section is comprised entirely of elastic scattering, capture, and fission,  $\alpha$  describes much of the needed information about reactions on  $^{233}\text{U}$ . Further, because it is a ratio, it is often both much simpler and more reliable to determine experimentally as many of the factors contributing to the systematic uncertainties, such as sample mass, self-shielding, and

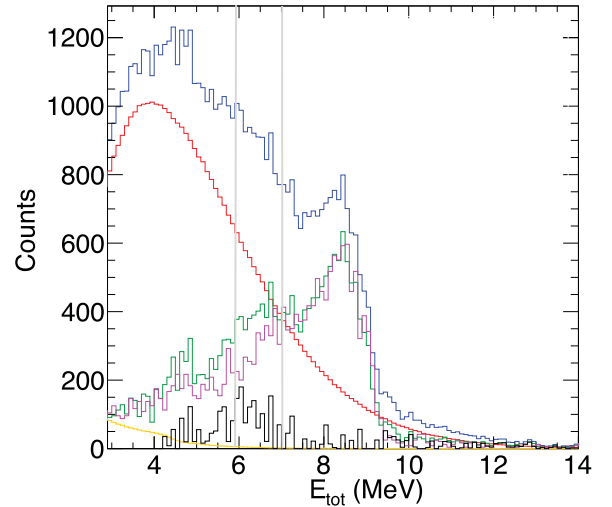


FIG. 8. Background components as a function of the total energy of the  $\gamma$  rays for neutrons with an incident energy of 300 eV. The total number of events (blue line), the scaled fission background (red line), the fission background suppress (green line), the scaled scatter background (magenta line), the scaled delay  $\gamma$  background (yellow line), and the capture events (black line) are here represented. The gray lines delimit the energy region around the  $Q$  value for capture reactions on  $^{233}\text{U}$  that has been used to identify the capture events.

neutron exposure, will cancel out in a appropriately designed experiment. Experimentally, a number of events  $C_i(E_n)$  is measured as a function of neutron energy that is associated with process  $i$  (fission or capture in this case):

$$C_i(E_n) = \varepsilon_i Y_i(E_n) \quad (5)$$

and

$$Y_i(E_n) = \sigma_i(E_n) N_{^{233}\text{U}} \Phi_n(E_n), \quad (6)$$

where  $\varepsilon_i$  is the efficiency of detecting an event of type  $i$ ,  $Y_i(E_n)$  is the total yield of events of type  $i$  for a  $^{233}\text{U}$  sample smaller than the neutron beam,  $N_{^{233}\text{U}}$  is the total number of atoms of  $^{233}\text{U}$  in the sample, and  $\Phi_n(E_n)$  is the total number of neutrons per unit area the sample was exposed to over the course of the experiment. Then to determine  $\alpha$  we have

$$\frac{C_\gamma(E_n)}{C_f(E_n)} = \frac{\varepsilon_\gamma Y_\gamma(E_n)}{\varepsilon_f Y_f(E_n)} \quad (7)$$

$$= \frac{\varepsilon_\gamma \sigma_\gamma(E_n) N_{^{233}\text{U}} \Phi_n(E_n)}{\varepsilon_f \sigma_f(E_n) N_{^{233}\text{U}} \Phi_n(E_n)} \quad (8)$$

$$= \frac{\varepsilon_\gamma \sigma_\gamma(E_n)}{\varepsilon_f \sigma_f(E_n)} \quad (9)$$

$$= k \frac{\sigma_\gamma(E_n)}{\sigma_f(E_n)} \quad (10)$$

$$= k\alpha(E_n), \quad (11)$$

therefore

$$\alpha(E_n) \equiv \frac{1}{k} \frac{C_\gamma(E_n)}{C_f(E_n)}, \quad (12)$$

where, assuming the detection efficiencies  $\varepsilon_\gamma$ ,  $\varepsilon_f$  for capture and fission do not depend on the neutron energy,  $k$  is an

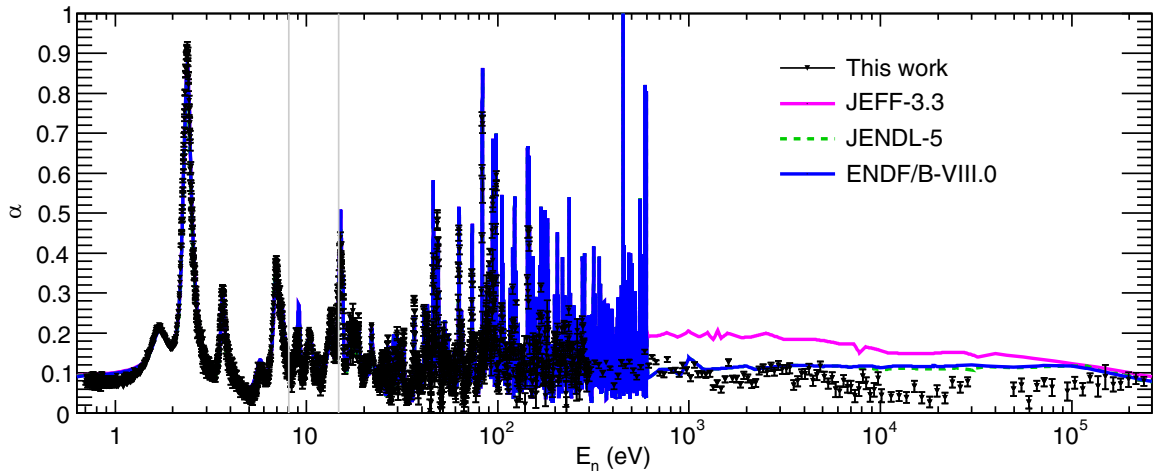


FIG. 9. Capture-to-fission ratio on  $^{233}\text{U}$  (black) compared with ENDF/B-VIII.0 (blue), JEFF-3.3 (magenta), and JENDL-5 (green). The results are shown using 1000 bins/decade from 0.7–100 eV, 500 bins/decade from 100–300 eV, 50 bins/decade from 300–10000 eV, and 25 bins/decade from 100–250 keV. The normalization region is indicated by gray lines. The error bars represent the statistical uncertainties.

energy-independent constant. If the capture and fission cross sections are known at a particular energy or over an energy range,  $k$  can be trivially determined from the ratio of detected events over that energy range, and the ratio  $\alpha(E_n)$  can be determined directly from the measured data over the full energy range of the measurement.  $C_\gamma(E_n)$  was determined based on events with multiplicities 4 and 5, and  $E_{\text{sum}}$  from 5.9–7.0 MeV as discussed in Sec. III E.  $C_f(E_n)$  was determined by the number of events in the window with cluster multiplicities from 8 to 14 and  $E_{\text{sum}}$  from 0–14 MeV, a region where only fission contributes to the DANCE response.

#### F. Uncertainty quantification

The statistical uncertainties were propagated during the data analysis. The systematic uncertainty obtained from the scattering normalization factor is 2%. There is some uncertainty related to the ENDF/B-VIII.0 capture and fission cross section used to normalize the ratio, however the information in the normalization energy region was not provided in the covariance matrix from the ENDF/B-VIII.0 database. Therefore this work relies on the covariance matrix from ENDF/B-VII.1 to calculate the systematic uncertainties coming from the use of the evaluations to normalize the ratio, which are 6.3%. No major differences have been found comparing the fission and capture cross section from both versions except for small differences, mainly in the capture cross section, due to updates in the thermal region.

### IV. RESULTS

#### A. Capture-to-fission ratio results

The capture-to-fission ratio is reported with resolution matched to a combination of the experimental resolution and the statistical uncertainty. Thus, 1000 bins/decade were used in the resolved resonance region from 0.7 to 100 eV, 500 bins/decade from 100 to 300 eV, 50 bins/decade from 300 eV to 10 keV, and 25 bins/decade from 10 to 250 keV.

In order to calculate the normalization factor ( $k$ ) representing the ratio of the detectors efficiencies, a broadened fission and capture cross section must be used. The broadened cross section includes effects of the resolution function of the facility, and include the shape of the beam pulse, the neutron moderator and the Doppler broadening.

The code SAMMY [17] was used to broaden the ENDF/B-VIII.0 capture and fission cross sections. The neutron energy region selected to normalize the experimental data is between 8.1–14.7 eV [18], see Fig. 9. The normalization factor ( $k$ ) from Eq. (12), was calculated from the integrals of the ENDF/B-VIII.0 broadened cross sections, which are given in Table II, being equal to  $6.84 \pm 0.01$ .

ENDF/B-VIII.0 used the resonance parameters from ENDF/B-VII.0. Those parameters include transmission [5] and fission cross section data [19] measured at the Oak Ridge Electron Linear Accelerator (ORELA), in addition to other experimental data which were not specified. The high resolution capture-to-fission data presented in this work provide more direct information on the capture reaction in the resonance region to calculate the resonance parameters in a new evaluation.

The ENDF/B-VIII.0 cross section ratio is in agreement with the general trend of this data in the resolved resonance region. However, some discrepancies are found in the shape and number of resonances, see Fig. 10, where a weak enhancement not present in the evaluation can be observed in these experimental data. In the unresolved resonance region, the ENDF/B-VIII.0 evaluation and JEFF-3.3 are in disagreement.

TABLE II. ENDF/B-VIII.0 broadened cross sections integrals in the energy range from 8.1–14.7 eV selected for normalization.

Evaluation	Reaction	Integral (eV b)
ENDF/B-VIII.0	$(n, \gamma)$	106.8
ENDF/B-VIII.0	$(n, f)$	682.2

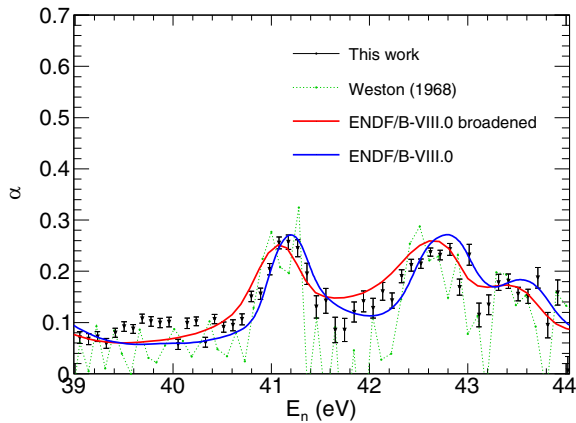


FIG. 10. This work compared to the ENDF/B-VIII.0 cross section ratio and the experimental data from [2] in the neutron energy range from 39 to 44 eV showing some discrepancies between this data and the evaluation. The effect of the broadening can be clearly observed in this figure.

ENDF/B-VIII.0 is the evaluation in better agreement with this work. A lower cross section ratio is observed between 10 keV and 150 keV than past evaluations, see Fig. 9.

This work provides higher resolution data in the resolved resonance region than previous measurements. It is also the first measurement between 2 and 30 keV, extending the experimental information to higher energies in the unresolved resonance region.

Besides the previously mentioned discrepancies between this work, the existing experimental data, and the evaluations there are some other differences, as observed in the shape of the ratio, see Figs. 11 and 12. Structures clearly distinguished in the data from Weston *et al.* [2], are not observed in this and previous works or in the ENDF/B-VIII.0 evaluation, see Fig. 12. The first of these structures found at 11.8 eV in the data from Weston *et al.* [2] was identified in their work as a possible platinum impurity in the sample generating a resonance in the capture cross section.

The high-resolution dataset from Berthoumieux *et al.* [1] extends up to 20 eV. Above this energy and below 30 keV,

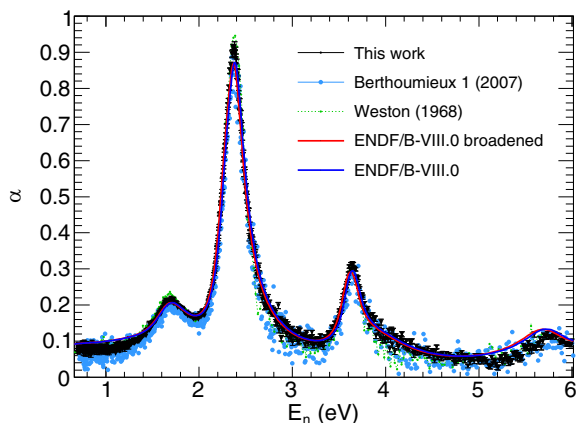


FIG. 11. This work compared to the experimental data from [1,2] and the evaluations in the energy region from 0.7–6 eV.

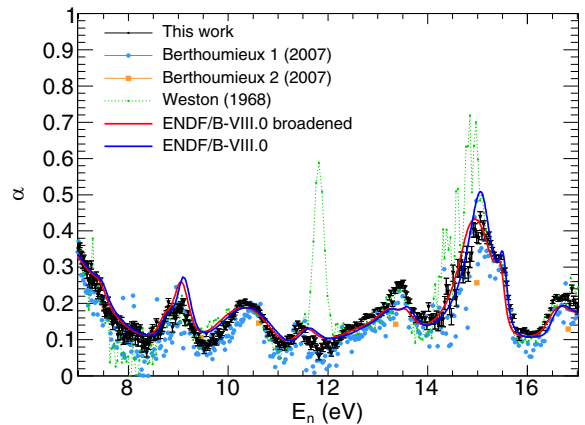


FIG. 12. This work compared to ENDF/B-VIII.0 and the experimental data from Weston *et al.* [1] and Berthoumieux *et al.* [2] in the energy region from 7–17 eV showing a structure in the data from Weston *et al.* that is not observed in the present work or in the work from Berthoumieux *et al.*

only the data from Weston *et al.* [2] are provided with high resolution, while Berthoumieux *et al.* [1] provides 20 bins per decade up to 1 keV. In this energy region, structures at 67, 222, and 228 eV reported in the data from Weston *et al.* [2] are not observed in the present work, supporting the ENDF/B-VIII.0 evaluation. The low-resolution data by Berthoumieux *et al.* [1] confirms the absence of the first structure, providing no information about the second and third one, see Fig. 13.

Above 150 eV the statistical fluctuations in the data from Weston *et al.* [2] are too large for a reliable description of the cross section ratio. Also, above 300 eV and all along the transition from the resolved to the unresolved resonance region, the data from Berthoumieux *et al.* [1] are below the remaining datasets. The lower resolution reported by the present work compared to Weston *et al.* [2] provides a smoother cross section ratio in that region, while providing a detailed

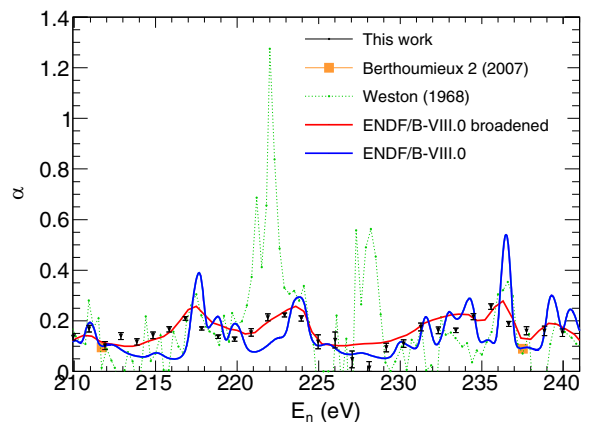


FIG. 13. This work compared to ENDF/B-VIII.0 and the experimental data from [1,2] in the energy region from 210–240 eV. The structures found at 222 and 228 eV in the data from Weston is not observed in this work. The effect of the broadening can be clearly observed in this figure.



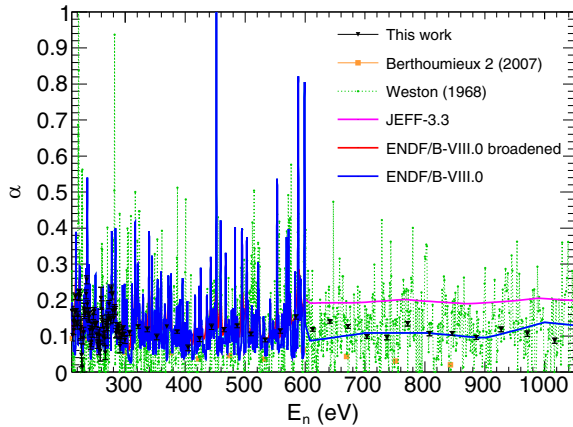


FIG. 14. This work compared to the experimental data from [1,2], and the ENDF/B-VIII.0 and JEFF-3.3 evaluations in the energy region from 200–1400 eV, showing the transition from the resolved to the unresolved resonance region.

description of the shape of the ratio, see Fig. 14. Above 2 keV up to 30 keV there are no data of the capture-to-fission ratio in EXFOR. This the first measurement provided in this energy range. Figure 15 presents this work compared to Weston et al. [2] and the ENDF/B-VIII.0 and JEFF-3.3 evaluations from 1 to 3 keV. ENDF/B-VIII.0 and JENDL-5 are the same in this region, so only ENDF/V-VIII.0 and JEFF-3.3 are shown in Fig. 15. Both are in good agreement with the present data. JEFF-3.3 is systematically higher than the experimental data in this region.

Above 10 keV and up to 150 keV, a lower capture-to-fission ratio is observed in this work than predicted in any evaluation. No data are reported in this work from 30 keV to 48 keV. In that energy region there was a reduction of the neutron flux due to the aluminum absorption dip. Above 150 keV, the ENDF/B-VIII.0 and JENDL-5 evaluations are in good agreement with this work and Hopkins and Diven [3], see Fig. 16.

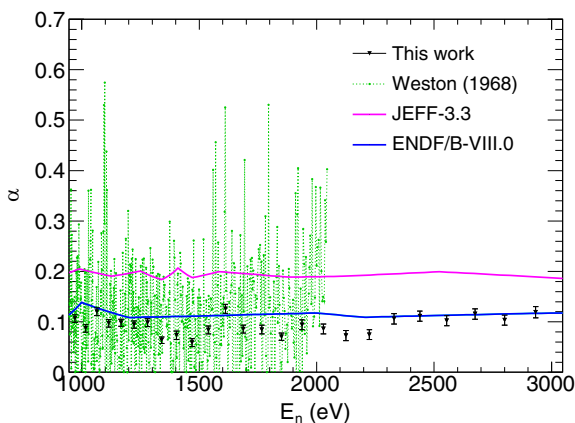


FIG. 15. This work compared to the experimental data from [2], and the ENDF/B-VIII.0 and JEFF-3.3 evaluations in the energy region from 1–3 keV, showing the good agreement between this work and ENDF/B-VIII.0.

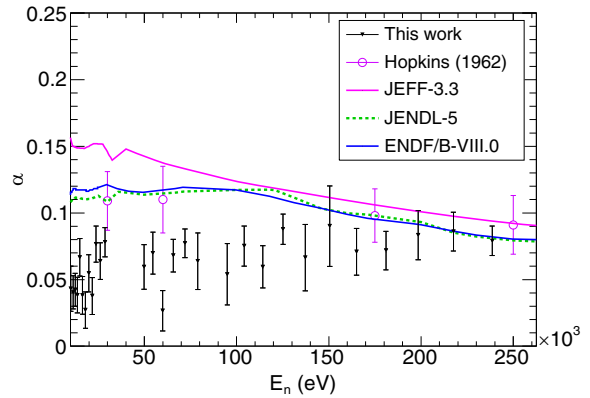


FIG. 16. This work compared to [3], and the evaluations in the energy region from 10–250 keV. This work presents a lower capture-to-fission ratio than the evaluations and Hopkins and Diven [3] below 150 keV, and a good agreement within the uncertainties at higher energies.

## B. Capture cross section results

The capture cross section is presented for comparison in Fig. 17. It was calculated by multiplying the capture-to-fission ratio result by the ENDF/B-VIII.0 fission cross section. The ENDF/B-VIII.0 broadened cross section was used in the resolved resonance region for the calculation. We remind the reader that this work is not an independent measure of the capture cross section.

## V. STATISTICAL MODEL CALCULATION

Statistical model calculations for neutron induced reactions on  $^{233}\text{U}$  were performed with the CoH<sub>3</sub> code [20] from 1 keV up to 5 MeV, energy for which only the first fission chance is involved. The CoH<sub>3</sub> code is particularly suitable for calculating the reaction cross section on deformed nuclei, as it properly combines the coupled-channels optical model and the statistical Hauser-Feshbach model calculations by performing the Engelbrecht-Weidenmüller transformation [21–23] of the penetration matrix. Coupled-channel calculations were performed with five levels from  $5/2^+$  to  $13/2^+$  by using Soukhovitskii’s optical model parametrization [24] together with the deformation parameters from the Finite Range Droplet Model (FRDM) [25]. Since the deformation parameters are different from those employed in the analysis by Soukhovitskii *et al.*, especially because FRDM predicts rather larger  $\beta_4$  of 0.12, we take the parameters as the initial value, and adjust them to better reproduce the total cross section data of  $^{233}\text{U}$ .

Since the evaluation of the fission cross section in the ENDF/B-VIII which was taken from JENDL-4.0 is based on a large number of experimental fission data that include both the absolute measurement and the ratio to other fissioning systems, we adjust the fission barriers to reproduce the ENDF fission cross section. The other model parameters, such as the level density and the giant dipole resonances, are the same as the previous studies [26,27]. Although the giant resonances are kept fixed, we can still try different values of the average

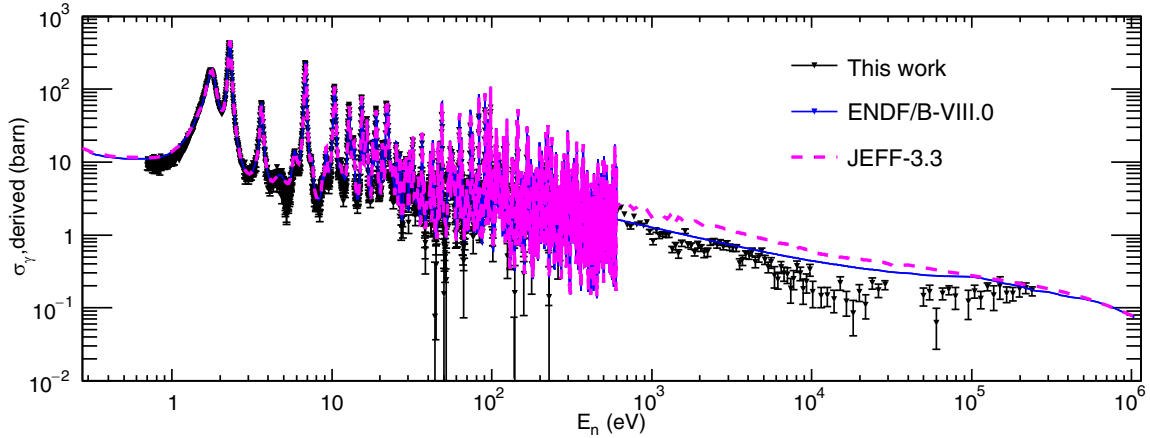


FIG. 17. The  $^{233}\text{U}(n, \gamma)$  cross section calculated multiplying the capture-to-fission cross section ratio by the ENDF/B-VIII.0 fission cross section. The broadened cross section has been used in the resolved resonance region. The results are compared with the ENDF/B-VIII.0 and JEFF-3.3 evaluations. The error bars represent the statistical uncertainties.

$\gamma$ -ray width  $\langle \Gamma_\gamma \rangle$  by adjusting the  $M1\gamma$ -ray strength function for the scissors mode [27]. Mughabghab's compilation [28] gives 40 meV. A prediction by the  $M1$  systematic study [27] is 31 meV. When we roughly estimate by fitting to the data of Hopkins and Diven [3], it yields 24 meV. Finally, we have eliminated the scissor mode in the 16 meV calculation.

The calculated ratios of neutron capture cross section to fission ( $\alpha$  value) are shown in Fig. 18, where the four different curves clearly demonstrate how the calculated results are sensitive to the average  $\gamma$ -ray width employed. The difference in  $\langle \Gamma_\gamma \rangle$  changes the magnitude of the  $\alpha$  value, while the shape stays similar. For example, a 20% increase in  $\langle \Gamma_\gamma \rangle$  makes a 16% increase in the capture cross section at 1 keV, while it slightly decreases the fission cross section by 1.5%. Therefore the calculated  $\alpha$  value is roughly proportional to  $\langle \Gamma_\gamma \rangle$ . Since the statistical Hauser-Feshbach gives resonance-average cross sections, extrapolation into the resolved resonance region is not so meaningful. However, the calculated cross section ratio

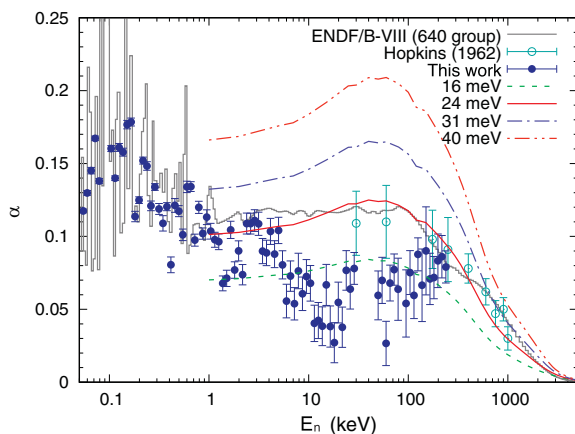


FIG. 18. Statistical model calculations for the neutron-induced reaction on  $^{233}\text{U}$  and comparison of experimental data. The four curves are for different average  $\gamma$ -ray width of 16, 20, 24, and 40 meV.

still represents the average properties of resolved resonances, because the kinetic factor of  $\pi/k_n^2$ , where  $k_n$  is the incident-neutron wave number, cancels out in the ratio. The  $\alpha$  value is calculated as the ratio of the average capture width to the fission width, and it asymptotically approaches a constant. The 40 meV calculation below 1 keV, which gives  $\alpha = 0.164$ , indeed represents the average in the resonance region.

However, the 40 meV calculation disagrees with both the present experimental data as well as the data by Hopkins and Diven [3]. To reproduce the data of Hopkins and Diven, we need to reduce  $\langle \Gamma_\gamma \rangle$  to 24 meV, which is about half of the resonance analysis value. It should be noted that although the 24 meV calculation is also consistent with the evaluated data, the evaluation was actually adjusted to Hopkins and Diven [3], which implies that the authors of the evaluation also needed to use an inconsistent  $\langle \Gamma_\gamma \rangle$  from the resonance analysis.

The present experimental data above 1 keV are lower than the evaluation, and to reconcile the difference between the measured and calculated  $\alpha$  values,  $\langle \Gamma_\gamma \rangle$  needs to be even smaller. The 16 meV calculation without the  $M1$  scissors mode roughly represents the magnitude of measurements, although a large deviation still persists. The asymptotic ratio of 0.0695 significantly differs from the 40 meV calculation. Even though we explored this possibility within a reasonable parameter space, it was difficult to reproduce the fission and  $\alpha$  data simultaneously in the current reaction modeling. At this time this behavior is not fully understood and further studies are needed to better understand the large difference between the experiment data and the theoretical calculation in this energy region.

## VI. IMPACT ON THE Th-U FUEL CYCLE

While specific impacts of a cross section for the Th/U fuel cycle will depend on the specifics of an individual reactor design or model which are beyond the scope of this manuscript, we comment briefly on the general trends that this measurement would favor. From Eq. (1), one can see that the  $^{233}\text{U}$  is made from neutron capture reactions on  $^{232}\text{Th}$  after

a series of  $\beta$  decays. Since the  $^{232}\text{Th}$  fission threshold is at about 1 MeV, the majority of neutrons below 1 MeV only produce significant energy from fission based on  $^{233}\text{U}$  fission. Any fission from  $^{233}\text{U}$  will produce energy and more neutrons while any capture on  $^{233}\text{U}$  both removes neutrons and fissile material from the system, reducing the efficiency of the energy production. The broad confirmation of the evaluated cross sections below 10 keV will leave energy production in these regions unchanged, while the lowered measured cross section ratio for energies between 10–150 keV would be expected to slightly increase the energy production efficiency in systems with significant neutron fluxes in this energy regime.

## VII. CONCLUSIONS

The capture-to-fission cross section ratio was measured at LANSCE using a setup combining DANCE to measure  $\gamma$  rays coming from capture and fission reactions, and NEUANCE to measure fission neutrons. Fission  $\gamma$ -rays identification was performed by searching for coincidences between these two detectors. Results of the capture-to-fission ratio are provided for incident neutron energies from 0.7 eV to 250 keV. The result was normalized to the ENDF/B-VIII.0 broadened capture-to-fission cross section ratio in the neutron energy region between 8.1 and 14.7 eV. This is the first measurement provided between 2 and 30 keV. The evaluations are in good agreement with the results in the resolved resonance

region while this work shows a lower capture-to-fission ratio in the unresolved resonance region from 10 to 150 keV, where large discrepancies are found within the evaluated data. Some discrepancies were found between this work and the existing experimental data and evaluations in the number of resonances and their shape. Above 10 keV and up to 150 keV, a lower capture-to-fission ratio is observed in this work with respect to the evaluations and the data from Hopkins and Diven [3]. Comparison of this work with statistical model calculations show that a smaller  $\langle\Gamma_\gamma\rangle$  than obtained from a resonance evaluation was needed to reproduce the unresolved data, indicating future work is needed.

## ACKNOWLEDGMENTS

This work was supported by the Nuclear Criticality Safety Program (NCSP), funded and managed by the National Nuclear Security Administration for the Department of Energy. This work benefited from the use of the Los Alamos Neutron Science Center and was supported by the US Department of Energy through the Los Alamos National Laboratory. Los Alamos National Laboratory is operated by Triad National Security, LLC, for the National Nuclear Security Administration of US Department of Energy (Contract No. 89233218CNA000001). The isotope(s) used in this research was supplied by the US Department of Energy Isotope Program, managed by the Office of Isotope R&D and Production.

- 
- [1] E. Berthoumieux, U. Abbondanno, G. Aerts, H. Álvarez, F. Álvarez-Velarde, S. Andriamonje, J. Andrzejewski, P. Assimakopoulos, L. Audouin, G. Badurek *et al.*, *Proceedings of the International Conference on Nuclear Data for Science and Technology* (EDP Sciences, 2008), pp. 571–574.
- [2] L. W. Weston, R. Gwin, G. deSaussure, R. R. Fullwood, and R. W. Hockenbury, *Nucl. Sci. Eng.* **34**, 1 (1968).
- [3] J. C. Hopkins and B. C. Diven, *Nucl. Sci. Eng.* **12**, 169 (1962).
- [4] M. T. Pigni, R. Capote, and A. Trkov, *Annals of Nuclear Energy*, **163**, 108595 (2021).
- [5] K. H. Guber, *Nucl. Sci. Eng.* **135**, 141 (2000).
- [6] M. Bacak, M. Aiche, G. Bélier, E. Berthoumieux, M. Diakaki, E. Dupont, F. Gunsing, J. Heyse, S. Kopecky, M. Krťicka *et al.*, *EPJ Web Conf.* **239**, 01043 (2020).
- [7] P. W. Lisowski, C. D. Bowman, G. J. Russell, and S. A. Wender, *Nucl. Sci. Eng.* **106**, 208 (1990).
- [8] D. Habs, F. S. Stephens, and R. M. Diamond, Technical Report No. PUB-5020-2, Lawrence Berkeley Laboratory, 1979.
- [9] M. Heil, R. Reifarh, M. Fowler, R. Haight, F. Käppeler, R. Rundberg, E. Seabury, J. Ullmann, J. Wilhelmy, and K. Wisshak, *Nucl. Instrum. Methods Phys. Res. A* **459**, 229 (2001).
- [10] M. Jandel, B. Baramsai, T. Bredeweg, A. Couture, A. Favalli, A. Hayes, K. Ianakiev, M. Iliev, T. Kawano, S. Mosby *et al.*, *Nucl. Instrum. Methods Phys. Res. A* **882**, 105 (2018).
- [11] S. Ritt and P.-A. Amaudruz, MIDAS - maximum integrated data acquisition system, [https://daq00.triumf.ca/MidasWiki/index.php/Main\\_Page](https://daq00.triumf.ca/MidasWiki/index.php/Main_Page).
- [12] Dance digital data acquisition system (2019), [https://github.com/lansce-nuclear-physics/DANCE\\_Acquisition](https://github.com/lansce-nuclear-physics/DANCE_Acquisition).
- [13] S. Mosby, F. Tovesson, A. Couture, D. Duke, V. Kleinrath, R. Meharchand, K. Meierbachtol, J. O'Donnell, B. Perdue, D. Richman *et al.*, *Nucl. Instrum. Methods Phys. Res. A* **757**, 75 (2014).
- [14] Dance data analysis software (2019), [https://github.com/lansce-nuclear-physics/DANCE\\_Analysis](https://github.com/lansce-nuclear-physics/DANCE_Analysis).
- [15] M. Jandel, T. A. Bredeweg, A. Couture, M. M. Fowler, E. M. Bond, M. B. Chadwick, R. R. C. Clement, E.-I. Esch, J. M. O'Donnell, R. Reifarh *et al.*, in *The Applications of Accelerators in Research and Industry—Proceedings of the Nineteenth International Conference on the Application of Accelerators in Research and Industry*, edited by F. D. McDaniel, B. L. Doyle, I. Ben-Itzhak, R. W. Hamm, B. M. Johnson, J. M. Sisterson, D. R. Slaughter, S. Thevuthasan, G. Vizkelethy, Y. Wany *et al.* (Elsevier, New York, 2007), Vol. 261, pp. 1117–1121.
- [16] L. Zavorka, M. J. Mocko, and P. E. Koehler, *Nucl. Instrum. Methods Phys. Res. A* **901**, 189 (2018).
- [17] N. M. Larson, Updated Users' Guide for SAMMY: Multi-level R-Matrix Fits to Neutron Data. Using Bayes' Equations, ORNL/TM-9179/R8, ENDF-364/R2, Oak Ridge National Lab. (ORNL), Oak Ridge, USA, 2008.
- [18] G. Noguere, O. Cabellos, D. Neudecker, A. Trkov, and R. Capote, Technical Report No. INDC(NDS)-0835, International Atomic Energy Agency (IAEA), 2022.

- [19] K. H. Guber, R. R. Spencer, L. C. Leal, P. E. Koehler, J. A. Harvey, R. O. Sayer, H. Derrien, T. E. Valentine, D. E. Pierce, V. M. Cauley *et al.*, *Nucl. Sci. Eng.* **139**, 111 (2001).
- [20] T. Kawano, in *Proceedings of the 6th International Workshop on Compound-Nuclear Reactions and Related Topics CNR\*18 LBNL, Berkeley, CA, USA, September 24-28, 2018*, edited by J. Escher, Y. Alhassid, L.A. Bernstein, D. Brown, C. Fröhlich, P. Talou, W. Younes (Springer, Cham, 2022), Vol. 254, pp. 27–34.
- [21] C. A. Engelbrecht and H. A. Weidenmüller, *Phys. Rev. C* **8**, 859 (1973).
- [22] T. Kawano, P. Talou, and H. A. Weidenmüller, *Phys. Rev. C* **92**, 044617 (2015).
- [23] T. Kawano, R. Capote, S. Hilaire, and P. Chau Huu-Tai, *Phys. Rev. C* **94**, 014612 (2016).
- [24] E. S. Soukhovitskii, R. Capote, J. M. Quesada, and S. Chiba, *Phys. Rev. C* **72**, 024604 (2005).
- [25] P. Möller, J. R. Nix, W. D. Myer, and W. J. Swiatecki, *At. Data Nucl. Data Tables* **59**, 185 (1995).
- [26] J. L. Ullmann, T. Kawano, B. Baramsai, T. A. Bredeweg, A. Couture, R. C. Haight, M. Jandel, J. M. O'Donnell, R. S. Rundberg, D. J. Vieira *et al.*, *Phys. Rev. C* **96**, 024627 (2017).
- [27] M. R. Mumpower, T. Kawano, J. L. Ullmann, M. Krtička, and T. M. Sprouse, *Phys. Rev. C* **96**, 024612 (2017).
- [28] S. F. Mughabghab, *Atlas of Neutron Resonances, Resonance Parameters and Thermal Cross Sections, Z=1–100* (Elsevier, New York, 2006).